Dissolution Chemistry and Biocompatibility of Single-Crystalline Silicon Nanomembranes and Associated Materials for Transient Electronics

Suk-Won Hwang,[†,♦] Gayoung Park,[‡,♦] Chris Edwards,[§] Elise A. Corbin,[∥] Seung-Kyun Kang,[†] Huanyu Cheng,[⊥] Jun-Kyul Song,[†] Jae-Hwan Kim,[†] Sooyoun Yu,[#] Joanne Ng,[‡] Jung Eun Lee,[‡] Jiyoung Kim,[‡] Cassian Yee,[¶] Basanta Bhaduri,[§] Yewang Su,[⊥,○] Fiorenzo G. Omennetto,[△] Yonggang Huang,[⊥] Rashid Bashir,[∥] Lynford Goddard,[§] Gabriel Popescu,[§] Kyung-Mi Lee,[‡,▼,*] and John A. Rogers[†,§,■,▼,*]

[†]Department of Materials Science and Engineering, Frederick Seitz Materials Research Laboratory, University of Illinois at Urbana—Champaign, Urbana, Illinois 61801, United States, [‡]Global Research Laboratory, Department of Biochemistry and Molecular Biology, Korea University College of Medicine, Seoul 136-713, Republic of Korea, [§]Department of Electrical and Computer Engineering and [∥]Department of Bioengineering, University of Illinois at Urbana—Champaign, Urbana, Illinois 61801, United States, [⊥]Department of Mechanical Engineering, Civil and Environmental Engineering, Center for Engineering and Health, and Skin Disease Research Center, Northwestern University, Evanston, Illinois 60208, United States, [#]Department of Chemical and Biomolecular Engineering,University of Illinois at Urbana—Champaign, Urbana, Illinois 61801, United States, [¶]Department of Melanoma Medical Oncology and Immunology, University of Texas MD Anderson Cancer Center, Houston, Texas 77054, United States, [○]Center for Mechanics and Materials, Tsinghua University, Beijing 100084, China, [△]Department of Biomedical Engineering, Tufts University, Medford, Massachusetts 02155, United States, and [■]Department of Chemistry, Mechanical Science and Engineering, and Beckman Institute for Advanced Science and Technology, University of Illinois at Urbana—Champaign, Urbana, Illinois 61801, United States. [♦]S.-W.H. and G.P. contributed equally. [▼]K.-M.L. and J.A.R. contributed equally.

ABSTRACT Single-crystalline silicon nanomembranes (Si NMs) represent a critically important class of material for high-performance forms of electronics that are capable of complete, controlled dissolution when immersed in water and/or biofluids, sometimes referred to as a type of "transient" electronics. The results reported here include the kinetics of hydrolysis of Si NMs in biofluids and various aqueous solutions through a range of relevant pH values, ionic concentrations and temperatures, and dependence on dopant types and concentrations. *In vitro* and *in vivo* investigations of Si NMs and other transient electronic materials demonstrate biocompatibility and bioresorption, thereby suggesting potential for envisioned applications in active, biodegradable electronic implants.

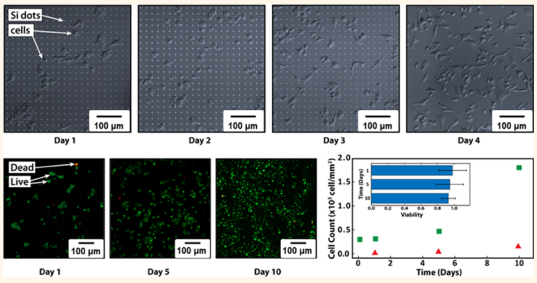

KEYWORDS: silicon nanomembranes · biocompatible · biodegradable · bioresorbable · transient electronics · hydrolysis

Developments in silicon-integrated circuits over the last several decades have led to their use in nearly every aspect of daily life. Historically, engineering emphasis has been placed on materials and designs optimized for reliable, high-performance operation. Time-invariant behavior is now possible over periods of time that can be measured in decades. Recent work demonstrates that the opposite behavior could also be of interest, in which the devices not only cease to function but also disappear completely over a well-defined but relatively short time frame, in a controlled fashion.[1−6] Potential applications range from temporary biomedical implants to resorbable environmental monitors, disposable electronics, and hardware-secure electronics. One class of such technology involves functional materials, substrates, and encapsulation layers that can dissolve or undergo hydrolysis in water or biofluids. Initial efforts on this particular form of "transient" electronics used ultra-small-scale components on water-soluble substrates[1,2] and, separately, resorbable organic electronic materials.[3−5] Recent advances establish routes to completely transient inorganic semiconductor devices and systems, with diverse, advanced modes of operation.[6−10] Here, the active semiconductor materials include options such as ultrathin Si and

* Address correspondence to jrogers@illinois.edu, kyunglee@korea.ac.kr.

Received for review February 11, 2014 and accepted March 31, 2014.

Published online 10.1021/nn500847g

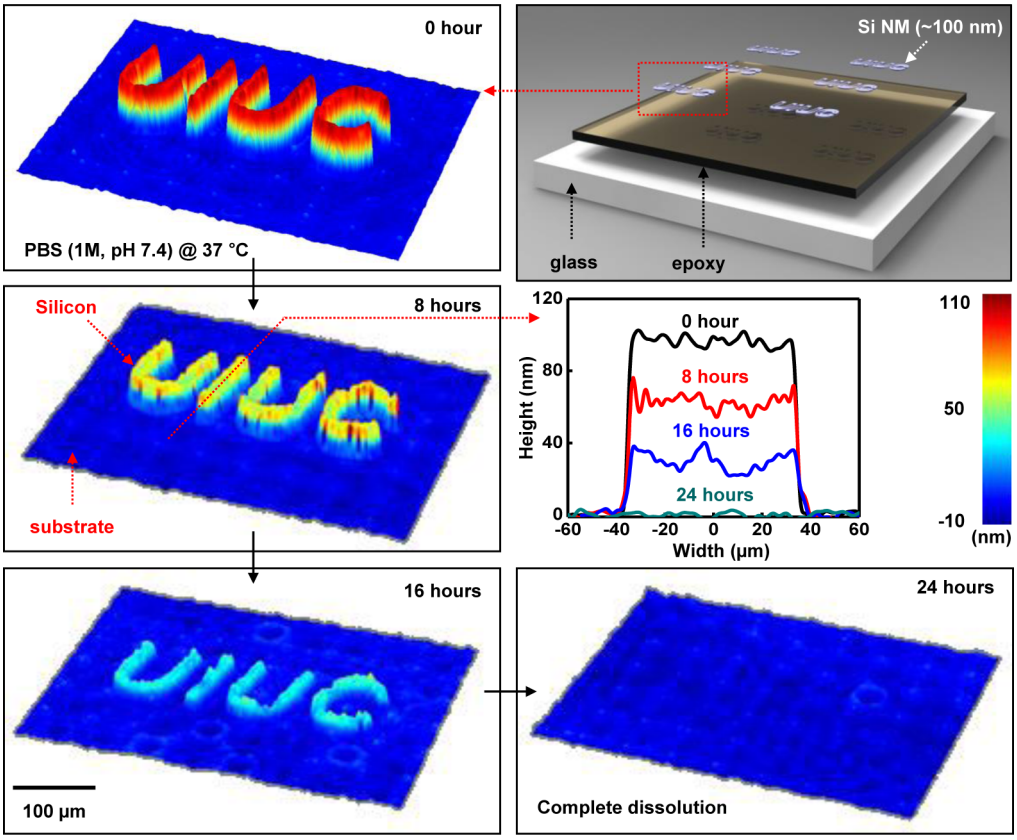

Figure 1. Dissolution behaviors of monocrystalline silicon nanomembranes (Si NMs, UIUC logo, ~100 nm thick) studied over large areas using a phase-sensitive microscopy technique for different times of immersion in phosphate buffer solution (PBS, 1 M, pH 7.4, Sigma-Aldrich, USA) at physiological temperature (37 °C): 0 (top left), 8 (middle left), 16 (bottom left), and 24 h (bottom right). Line scan profiles for each stage of measurements appear in the middle right. An exploded view schematic illustration of the test structure shows Si NMs on a film of epoxy on a glass substrate (top right).

ZnO; the gate/interlayer dielectrics include MgO and SiO_2; the metal interconnects and electrodes include Mg, Fe, W, and Zn. Substrates and encapsulation materials range from silk fibroin to polylactic-*co*-glycolic acid (PLGA), a copolymer of polylactic acid (PLA) and polyglycolic acid (PGA), PLA, polycaprolactone (PCL), and even rice paper. For high-performance electronics, as well as solar cells, photodetectors, and many other devices, monocrystalline silicon in the form of nanomembranes (NMs) represents the material of choice. The mechanisms and kinetics of dissolution and the biocompatibility of the Si NMs and their reaction products are all important due to the essential role of this class of material in semiconductor devices for potential applications in bioresorbable medical devices, eco-friendly electronics, and environmental sensors. Previous studies of hydrolysis in silicon have focused on material forms, such as quantum dots,[11,12] porous nanoparticles/membranes,[13−18] and bulk silicon,[18] that have little relevance to electronics but provide some context and findings on biocompatibility. The results presented here include detailed studies of mechanisms of hydrolysis of single-crystalline Si NMs under different conditions, measured using various modalities and assessed in both *in vitro* and *in vivo* toxicity studies.

RESULTS AND DISCUSSION

Previous work[6] revealed the kinetics of hydrolysis of Si NMs by use of a time sequence of thickness measurements performed using atomic force microscope (AFM) imaging on relatively small pieces of material (*e.g.*, several square micrometers) in simple, square geometries. Figure 1 illustrates a set of images obtained by transmission-mode laser diffraction phase microscopy (DPM)[19−21] of Si NMs (~100 nm thick) in large, complex patterns (UIUC text) evaluated at various times (0 h, top left; 8 h, middle left; 16 h, bottom left; 24 h, bottom right) of immersion in phosphate buffer solution (PBS, 1 M, pH 7.4, Sigma-Aldrich, USA) at physiological temperature (37 °C). Details of the DPM system appear in Supporting Information Figure S1 and the Methods section. The Si NM test structure used the top silicon layer of a silicon-on-insulator (SOI, SOITEC, France) thinned from 300 to 100 nm by repetitive thermal oxidation at 1100 °C, followed by wet chemical etching in hydrofluoric acid (HF, 49% electronic grade, ScienceLab, USA). Removal of the buried oxide by etching with HF released Si NMs from the SOI and enabled their transfer printing onto a spin-cast film of epoxy (SU-8 2, MicroChem, USA) on a glass substrate. Photolithography and reactive ion etching (RIE; Plasmatherm, USA)

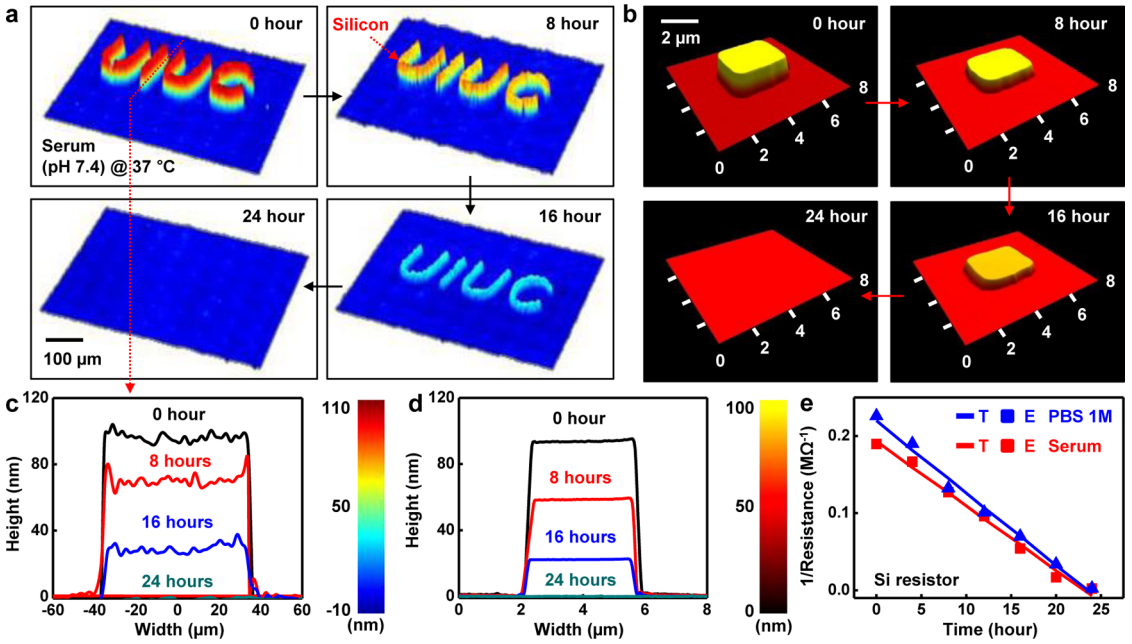

Figure 2. Images of Si NMs at various stages of dissolution in bovine serum (pH ~7.4) at physiological temperature (37 °C): 0 (top left), 8 (top right), 16 (bottom right), and 24 h (bottom left), measured by (a) DPM and (b) AFM. Thickness profiles extracted from the (c) DPM and (d) AFM images in (a) and (b) (0 h, black; 8 h, red; 16 h, blue; 24 h, dark cyan). (e) Theoretical (lines) and measured (symbols) changes in resistance of a serpentine shaped Si NM resistor after various times of immersion in PBS (blue, 1 M, pH ~7.4) and bovine serum (red, pH ~7.4) at body temperature (37 °C).

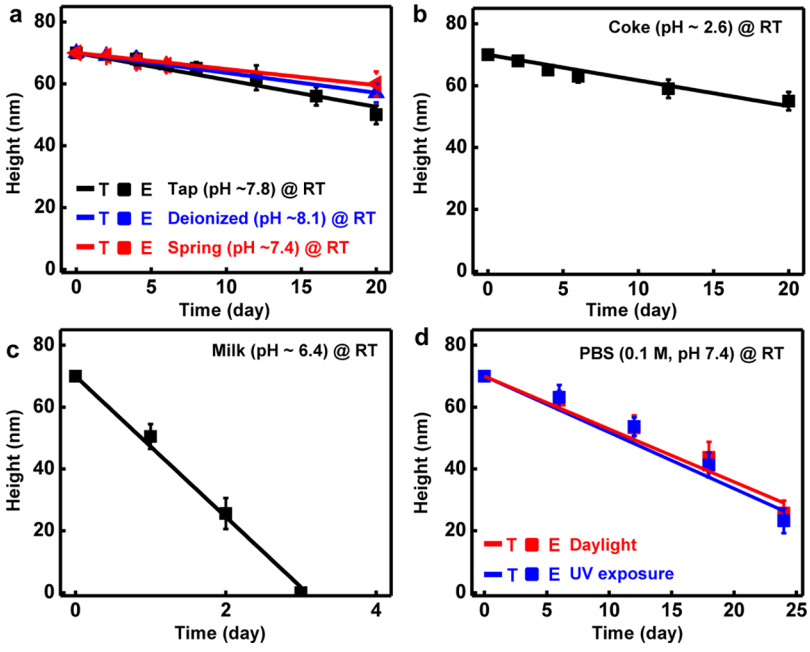

Figure 3. Theoretical (T, lines) and experimental (E, symbols) changes in thickness as a function of time for dissolution of Si NMs in various solutions. (a) Tap (pH ~7.8), deionized (DI, pH ~8.1) and spring (pH ~7.4) water, (b) Coke (pH ~2.6), and (c) milk (pH ~6.4) at room temperature. (d) Study of dissolution behavior during exposure to daylight (red) and UV light (blue).

with sulfur hexafluoride (SF_6) gas defined the "UIUC" pattern, as illustrated in the top right frame of Figure 1. Cross-sectional profiles (middle right) extracted from the DPM data indicate thicknesses of 97 ± 2.6 nm (0 h, black), 62 ± 3.4 nm (8 h, red), 29 ± 6.1 nm (16 h, blue) and 0 ± 1.5 nm (24 h, dark cyan). The results illustrate spatially uniform removal of silicon by hydrolysis, with well-defined linear kinetics, all of which are consistent with AFM results in Figure S2.

The dissolution behaviors of Si NMs are particularly important in biofluids relevant to envisioned applications in implantable biomedical devices. Figure 2a,b provides a set of images obtained by the DPM and AFM, during dissolution *via* hydrolysis in bovine serum

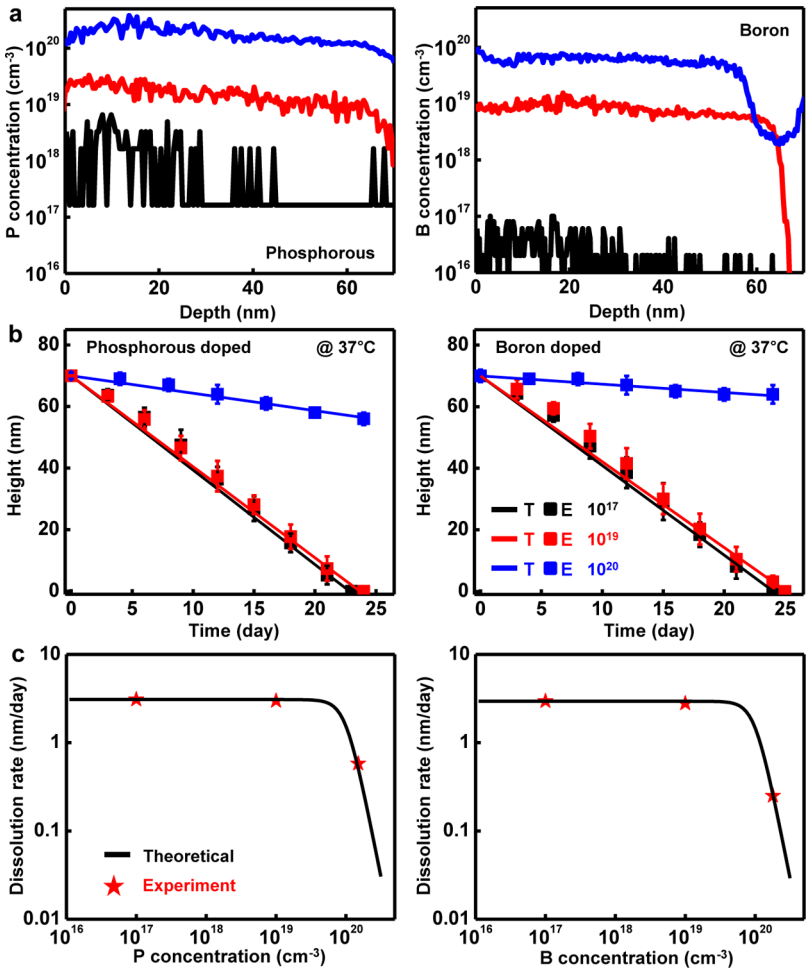

Figure 4. Kinetics of dissolution of phosphorus- and boron-doped Si NMs (3 μm $\times$ 3 μm $\times$ 70 nm) in aqueous buffer solution (0.1 M, pH 7.4) at physiological temperature (37 °C), as defined by the change in thickness as a function of time. (a) Dopant concentrations measured by secondary ion mass spectrometry (SIMS) for phosphorus (left) and boron (right). (b) Theoretical (T, lines) and experimental (E, symbols) results for the dissolution rates of Si NMs with different dopant concentrations (10^{17} cm^{-3}, black; 10^{19} cm^{-3}, red; 10^{20} cm^{-3}, blue) with phosphorus (left) and boron (right) during immersion in phosphate buffer solution (0.1 M, pH 7.4, Sigma-Aldrich, USA) at physiological temperature (37 °C). (c) Calculated (lines, black) and measured (stars, red) dissolution rates as a function of dopant concentration for phosphorus (left) and boron (right).

(pH ~7.4, Sigma-Aldrich, USA) at body temperature (37 °C), and corresponding thickness profiles extracted from each data are shown in Figure 2c,d. The results confirm dissolution rates in a range expected based on studies in PBS, with good levels of temporal and spatial uniformity. Additionally, measurements of the electrical resistance of a Si NM (lightly boron-doped, ~10^{16} /cm^3; resistivity, 10−20 Ω·cm) patterned into a meander shape and immersed in the same type of solution under the same conditions reveal results that match those based on expectation from the time-dependent changes in thickness (Figure 2e). Data from PBS solutions show the correspondence in rate. In all cases, the experiments involved removal of samples from solutions for measurements and then return to fresh solutions for continued dissolution.

The processes of hydrolysis depend critically on the chemical composition of the solution, the temperature, and the doping type and concentration for the Si NMs. Figure 3a summarizes dissolution rates measured by AFM at room temperature, in tap water (pH ~7.8), deionized (DI) water (pH ~8.1), and spring water (pH ~7.4). The results indicate rates in each case that are somewhat slower than those observed at similar pH levels using buffer solutions, likely due to the differences in ionic content. Dissolution in Coca-Cola (pH ~2.6, Figure 3b) and milk (pH ~6.4, Figure 3c) occurs at much faster rates than those of buffer solutions at similar pH. Techniques that use light exposure to etch semiconducting materials (*i.e.*, photoelectrochemical etching)[22−25] suggest the potential influence of light on the dissolution rate. To examine the possible effects, samples were immersed in PBS (0.1 M, pH ~7.4) at room temperature and exposed to natural daylight and ultraviolet light (UV, λ = 365 nm, I = 590 μW/cm^2 at a distance of 7 cm). No significant changes in dissolution rate were observed (Figure 3d). Such effects might be relevant at high levels of illumination, for example, from ~1 to ~500 mW/cm^2,[22−25] compared to those (590 μW/cm^2) examined here.

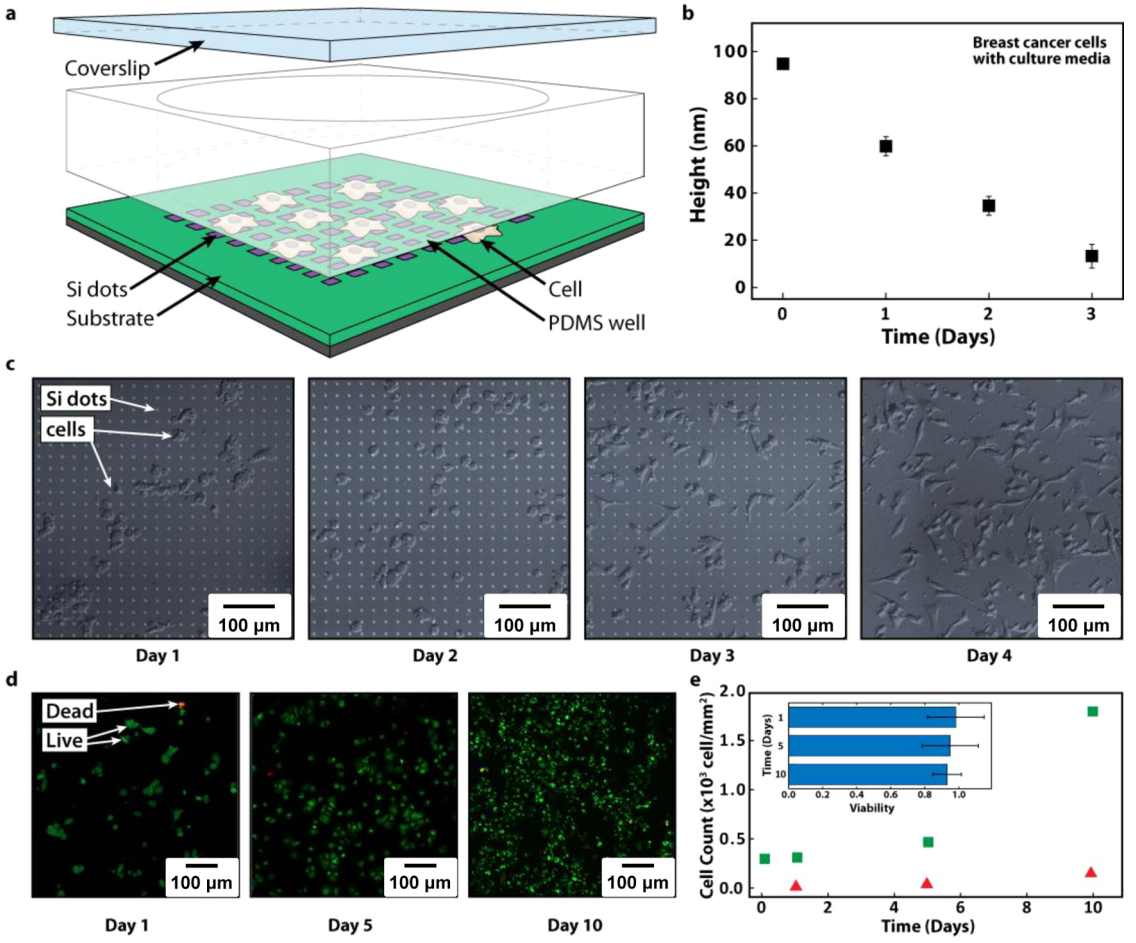

Figure 5. *In vitro* **cell culture evaluations of degradation and cytotoxicity associated with Si NMs. (a) Schematic illustration of the test structure for culturing cells on Si NMs. (b) Measured changes in thickness of the Si NMs during culture of breast cancer cells. (c) Differential interference contrast images showing the dissolution behaviors of Si NMs with adhered cells over 4 days, corresponding to the result in (b). (d) Set of fluorescent images describing cell viability using live/dead assay on Si NMs at days 1, 5, and 10. (e) Numbers of both live (green) and dead (red) cells over time as quantified from the live/dead assay in (d). As the cells divide, they increase in number and become more confluent, which also leads to an increase in the number of dead cells. The viability of cells over 1, 5, and 10 days, calculated as the fraction of total alive cells, appears in the inset.**

Types and concentrations of dopants in the Si NMs can be important. To examine the effects, Si NMs were doped with phosphorus and boron at three different concentrations (10^{17} cm^{-3}, black; 10^{19} cm^{-3}, red; 10^{20} cm^{-3}, blue) using spin-on-dopant (SOD, Filmtronics, USA) techniques. Depth profiles of the dopants evaluated by secondary ion mass spectrometry (SIMS) appear in Figure 4a. Figure 4b shows theoretical (T, lines; based on simple models of reactive diffusion described elsewhere)[6,26] and experimental (E, symbols) results of the dissolution kinetics for phosphorus-doped (left) and boron-doped (right) Si NMs in phosphate buffer solution (0.1 M, pH 7.4, Sigma-Aldrich, USA) at physiological temperature (37 °C), as measured by AFM. The results indicate a strong reduction of rate for dopant concentrations that exceed a certain level, such as 10^{20} cm^{-3}, as expected based on previous studies of silicon etching at comparatively high pH and temperature, for example, KOH (10−57%), NaOH (24%), ethylenediamine-based solution (EDP) at temperatures up to 115 °C.[27] Variations in rate (extracted from the theoretical results shown in Figure 4b) with dopant concentration appear in Figure 4c. The rate remains constant (R_i) up to a critical dopant concentration (C_0). Above C_0, a sharp decrease occurs, which is inversely proportional to the fourth power of the dopant concentration (C) consistent with a functional form established from studies of silicon under conditions of high pH[27]

$$R = \frac{R_i}{1 + (C/C_0)^4} \quad (1)$$

If $C_0 = 10^{20}$ cm^{-3} for both dopants and $R_i = 3.08$ and 2.95 nm/day for phosphorus and boron, respectively, then eq 1 yields results that agree well with measurements, as shown in Figure 4c. The large reduction for boron compared to that for phosphorus can be attributed, as in studies of traditional etching of silicon, to an absence of electrons in the conduction band at high boron concentration.[27] Similar behaviors can be revealed

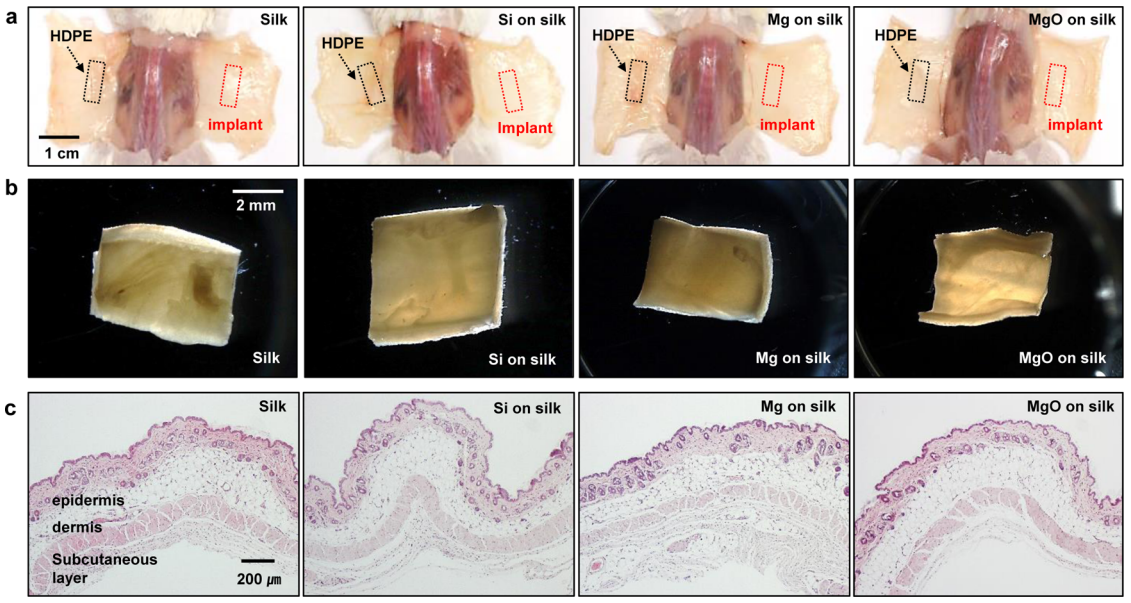

Figure 6. (a) Images of transient electronic test structures implanted in the subdermal dorsal region of BALB/c mice. (b) Microscopic images of representative skin tissues collected using a stereomicroscope. (c) H&E staining of skin sections from mice 5 weeks post implantation.

through electrical, rather than AFM, measurements of a phosphorus-doped Si NM (~35 nm) in a resistor configuration. Results appear in Figure S3a for similar solution conditions (0.1 M, pH 7.4, 37 °C). The surface chemistry of the phosphorus-doped Si NMs after immersion in buffer solution (0.1 M, pH 7.4, 37 °C) was examined by X-ray photoelectron spectroscopy (XPS). The results revealed no significant change in the chemistry (Figure S3b).

The nanoscale configurations of the Si NMs determine the time frames for complete dissolution as well as the total mass content of each element (*i.e.*, silicon, phosphorus, and boron for present purposes). For instance, the estimated dissolution time for a standard silicon wafer platform (~700 μm thickness) is several hundred years, based on the chemical kinetics observed in Si NMs studied here. The concentrations of the end products follow a similar scaling. A Si NM (1 mm $\times$ 1 mm $\times$ 100 nm) at high doping concentration (phosphorus/boron, doped with ~10^{20}/cm^3) dissolved in 1 mL of water yields concentrations of 0.2 ppm (ppm) for Si, 0.0005 ppm for phosphorus, and 0.0002 ppm for boron. These levels are well below natural physiological values. The corresponding concentrations for the case of a piece of a Si wafer with similar lateral dimensions would be thousands of times higher, with potential consequences on biological and/or environmental responses, depending on the application. Details appear in Table S1.

Many envisioned applications of silicon-based transient electronics require studies of biocompatibility. For *in vitro* assessment of the cytotoxicity and dissolution behaviors, cells from a metastatic breast cancer cell line (MDA-MB-231) were cultured on a patterned array of Si NMs using a PDMS-based microincubation chamber, as shown in Figure 5a. This breast cancer cell line is useful due to its rapid propagation and culture. Sterilizing and sealing the PDMS chamber against the solid substrate maintained appropriate conditions for the culture over multiple days. After culturing on the Si NMs for consecutive days, cells were removed from the surface using trypsin to allow measurement of changes in the thicknesses of the Si NMs by AFM (Figure 5b). The series of differential contrast images in Figure 5c illustrates the growth and proliferation behaviors of cells over the course of 4 days. The arrays of square Si NMs were no longer visible on the fourth day, consistent with the data of Figure 5b. Live/dead assays revealed viability at 1, 5, and 10 days, as determined by a set of fluorescent images of stained cells. Here, viable, living cells appear green; dead cells appear red. Figure 5e presents the change in numbers of live and dead cells; the inset shows the fraction of living cells as a measure of viability. Cell viability on days 1, 5, and 10 are 0.98 $\pm$ 0.11, 0.95 $\pm$ 0.08, and 0.93 $\pm$ 0.04, respectively. The slight increase in dead cells on days 5 and 10 is likely due to cell death that naturally occurs as a culture reaches confluency. Additional details on the cell culture and associated procedures appear in the Methods section.

In vivo toxicity and biodegradation studies of Si NMs as well as other transient electronic materials (silk, Mg, and MgO) are important for applications in temporary implants. Experiments were performed by implanting various test samples (silk, Si NMs on silk, Mg on silk, and MgO on silk) sterilized by exposure to ethylene oxide in the subdermal region of Balb/c mice in accordance with Institutional Animal Care and Use Committee (IACUC) protocols. The dorsal skin was

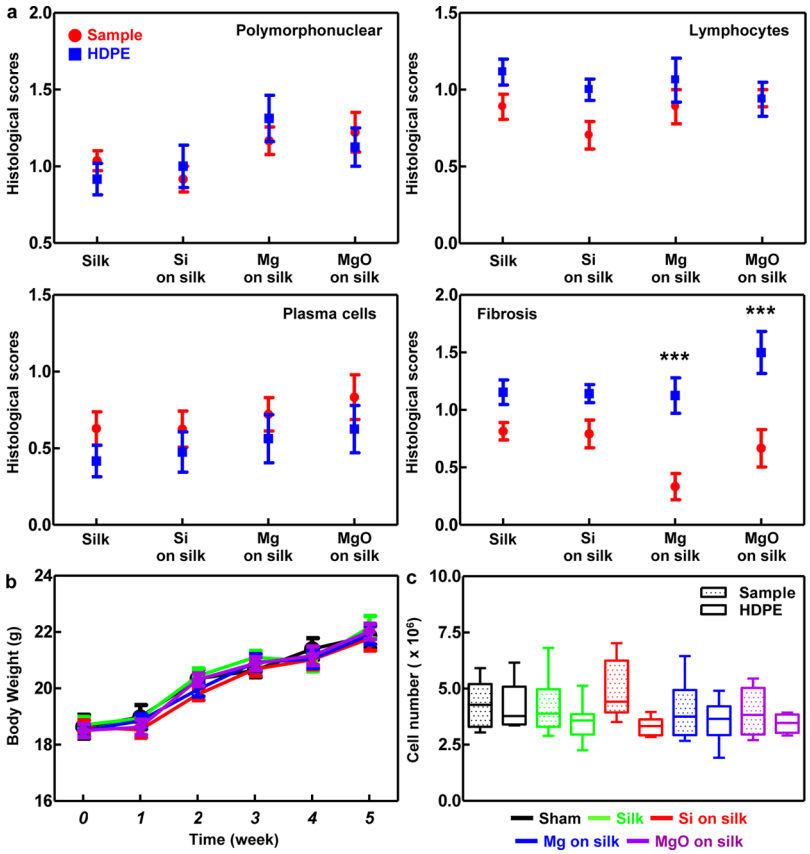

Figure 7. (a) Histological scores of tissues at the 5 week period based on H&E staining of skin sections from five groups of animals. (b) Body weight changes of mice implanted with sham-operated (black), silk (green), Si on silk (red), Mg on silk (blue), and MgO on silk (purple) after a 5 week implantation period (n = 8 per group). (c) Cell numbers in the axillary and branchial draining lymph nodes.

incised (~1 cm lengthwise) to create a subcutaneous pocket. Test samples along with control materials (high-density polyethylene (HDPE), FDA approved) were implanted into the pocket (Figure S4a). The skin incisions were closed with sterilized clips, and the mice were returned to the animal facility until analysis (Figure S4b). Figure 6a shows the dorsal view of mice subcutaneously implanted with transient samples, at 5 weeks post implantation. No residues were visible to the naked eye at the implant sites. Stereomicroscopic analysis confirmed no remaining materials within implanted sites (Figure 6b and Figure S5). Hematoxylin and eosin (H&E) staining and immunohistochemistry of skin sections demonstrated comparable levels of immune cells including polymorphonuclear cells (PMN), lymphocytes, and plasma cells to those of HDPE control groups (Figure 6c and Figure S6). The degree of fibrosis, measured by the thickness of collagen fibers, slightly increased in the HDPE-implanted tissue sections due to infiltration of collagen-producing fibroblasts at the implantation area (Figure 7a).[28] Such responses with silk and Si NMs on silk are comparable to those observed in the control HDPE, and both are somewhat higher than with samples of Mg on silk and MgO on silk. As compared to the sham-operated (*i.e.*, no implant) control group, no significant body weight loss was observed for mice in all cases during implantation period of 5 weeks (Figure 7b). In addition, there was no cytotoxicity of the four different types of samples observed by immunoprofiling using primary immune cells from the axillary and branchial draining lymph nodes (Figure 7c). Taken together, these results suggest the transient electronic materials examined here are biocompatible and have the potential to be used for long-term implantation, from months to years.

CONCLUSION

In summary, the nanoscale dimensions of Si NMs are critically important for use in transient, biocompatible electronics, simply due to their importance in defining the time scales for dissolution and the total mass content of the reaction products. Large-area studies of hydrolysis of Si NMs demonstrate spatially uniform, controlled dissolution in a wide range of aqueous solutions. Electrical measurements reveal results consistent with those determined by microscopy techniques. The dopant type and particularly the dopant concentration have strong influence on the rate, while exposure to light over ranges of intensity expected in envisioned applications does not. *In vitro* and *in vivo*

studies provide evidence for the biocompatibility of key materials for high-performance, inorganic transient electronics as subdermal implants. Further studies involving fully functional systems and in or on various other organs of the body will provide additional insights.

METHODS

Laser Diffraction Phase Microscopy System. The output of a 532 nm frequency-doubled Nd:YAG laser was coupled into a single-mode fiber and collimated to ensure full spatial coherence. This beam was aligned to the input port of a microscope. The collimated beam passed through the collector lens and focused at the condenser diaphragm, which was left open. The condenser lens created a collimated beam in the sample plane. Both the scattered and unscattered fields were captured by the objective lens and focused on its back focal plane. A beam splitter then redirected the light through a tube lens to create a collimated beam containing the image at the output image plane of the microscope. A diffraction grating placed at the output image plane of the microscope generated multiple copies of the image at different angles. Some of the orders were collected by a lens (L1) located a distance f_1 from the grating, to produce a Fourier transform of the image at a distance f_1 behind the lens. Here, the first-order beam was spatially filtered using a 10 μm diameter pinhole, such that after passing through the second lens (L2) this field approached a plane wave. This beam served as a reference for the interferometer. A large semicircle allowed the full zeroth order to pass through the filter without windowing effects. Using the zeroth order as the image prevented aberrations since it passed through the center of the lenses along the optical axis. A blazed grating was employed where the +1 order is brightest. In this way, after the filter, the intensities of the two orders were closely matched, ensuring optimal fringe visibility. A second 2f system with a different focal length was used to perform another spatial Fourier transform to reproduce the image at the CCD plane. The two beams from the Fourier plane formed an interferogram at the camera plane. The phase information was extracted via a Hilbert transform[19] to reconstruct the surface profile.[20,21]

Dissolution Experiments. To fabricate test structures (array of squares, 3 μm × 3 μm × 70−100 nm) of single-crystalline silicon nanomembranes, repetitive dry oxidation processes at 1100 °C followed by wet etching in hydrofluoric acid (HF, 49% electronic grade, ScienceLab, USA) reduced the thickness of the top silicon of a silicon-on-insulator (SOI, SOITEC, France) wafer. Doping with phosphorus and boron used a spin-on dopant (SOD, Filmtronics, USA) at different temperatures to control the concentrations (10^{16}/cm^3 to 10^{20}/cm^3). Patterned reactive ion etching (RIE, Plasmatherm, USA) with sulfur hexafluoride (SF6) gas defined Si NMs in square arrays. Samples were immersed in various solutions, including aqueous buffer solutions (Sigma-Aldrich, USA), tap/deionized (DI)/spring water, Coca-Cola, and milk at either room temperature or physiological temperature (37 °C). The samples were removed to measure the thickness of Si NMs by laser DPM and atomic force microscopy (AFM, Asylum Research MFP-3D, USA) and then reinserted into solutions, changed every 2 days.

Cell Culture Experiments. For seeding and culturing adherent cells on Si NMs, a 200 μL microincubation well was attached directly to each sample. To define the well, or culture chamber, a 6 mm dermal biopsy punch was pushed through a piece of polydimethylsiloxane (PDMS). The PDMS allowed for the culture well to be reversibly sealed with a coverslip for extended cultures at 37 °C. Prior to cell seeding, the sample was sterilized by filling the well with 70% ethanol. Highly metastatic human breast adenocarcinoma cells (MDA-MB-231 ATCC #HTB-26) were cultured in Leibovitz's L-15 medium (Sigma-Aldrich) with 10% fetal bovine serum and 1% penicillin−streptomycin. For seeding, cells were released from a T-25 flask with 0.25% trypsin−EDTA (Gibco). Cells were separated from the trypsin by centrifuging the suspension with 3−5 mL of medium for 6 min at 1000 rpm. The cells were then resuspended, diluted, and plated on the samples through the PDMS microincubation well at a density of 300 cells/mm^2. Cells were left to settle for 15 min, and then the well was sealed with a coverslip. The live/dead assay (Invitrogen, Carlsbad, CA) was employed to test cell viability after extended on-chip culture. Tested samples with adhered cells were incubated with 1 μM of acetomethoxy derivative of calcein (calcein AM, green; live) and 2 μM of ethidium homodimer (red; dead) for 35 min in phosphate buffered saline (PBS). The cells were then rinsed twice with PBS, and the samples were immediately imaged. Green fluorescence indicates that the cells are viable, whereas red marks dead cells. Images were used for counting and calculating the densities of cells in the fluorescein isothiocyanate (FITC, green; live) and the tetramethylrhodamine (TRITC, red; dead) channels. The ratio of integrated density in the FITC to TRITC channel defined the cell viability.

***In Vivo* Tissue Biocompatibility Tests.** Animal experiments were performed in accordance with the national and institutional guidelines and the Guide for the Care and Use Committees (KUIACUC-2013-93) of Laboratory Animals based on approved protocols by Korea University. Mice were anaesthetized by intraperitoneal injection of 30 mg/kg zolazepam hydroxide (Zoletil 50; Virbac, Sao Paulo, Brazil) and 10 mg/kg zylazine hydroxide (Rumpun; Bayer, Shawnee Mission, KS). The two sterile samples (one test and one control) were implanted subcutaneously into the dorsal pocket of mice for periods of 5 weeks. Mice were euthanized *via* CO_2 asphyxiation, and the implanted samples and surrounding tissue were excised. The tissue samples were fixed in 10% neutral buffered formalin, which were then embedded into paraffin, sliced at thickness of 4 μm, and stained with hematoxylin and eosin. The H&E-stained slices were imaged by optical microscopy. Images of the tissue were taken on a Leica M165 FC stereomicroscope equipped with a LEICA DFC310FX camera using the Leica application suite version 3.4.1 software program.

Statistics. All data are represented as mean ± SEM of three identical experiments made in three replicates. Statistical significance was determined by one-way analysis of variance (ANOVA) followed by Dunnett' multiple comparison test. Significance was ascribed at $p < 0.05$. All analyses were conducted using the Prism software (Graph Pad Prism 5.0).

Conflict of Interest: The authors declare no competing financial interest.

Acknowledgment. H.C. is a Howard Hughes Medical Institute International Student Research Fellow. The facilities for characterization and analysis were provided by the Material Research Laboratory and Center for Microanalysis of Materials at the University of Illinois at Urbana—Champaign, both of which are supported by the U.S. Department of Energy. The research was funded by an NSF INSPIRE grant. *In vivo* work was supported by Basic Science Research Program through the National Research Foundation of Korea (NRF) funded by the Ministry of Science, ICT & Future Planning (NRF-2007-00107 and NRF-2013M3A9D3045719) and the Converging Research Center Program (2013K000268).

Supporting Information Available: Supplementary Figures 1−6 and Table 1 provide additional information for the results described throughout the main text. This material is available free of charge *via* the Internet at http://pubs.acs.org.

REFERENCES AND NOTES

1. Kim, D.-H.; Kim, Y.-S.; Amsden, J.; Panilaitis, B.; Kaplan, D. L.; Omenetto, F. G.; Zakin, M. R.; Rogers, J. A. Silicon Electronics on Silk as a Path to Bioresorbable, Implantable Devices. *Appl. Phys. Lett.* **2009**, *95*, 133701.

2. Kim, D.-H.; Viventi, J.; Amsden, J.; Xiao, J.; Vigeland, L.; Kim, Y.-S.; Blanco, J. A.; Panilaitis, B.; Frechette, E. S.; Contreras, D.; *et al.* Dissolvable Films of Silk Fibroin for Ultrathin, Conformal Bio-Integrated Electronics. *Nat. Mater.* **2010**, *9*, 511–517.
3. Bettinger, C. J.; Bao, Z. Organic Thin-Film Transistors Fabricated on Resorbable Biomaterials Substrates. *Adv. Mater.* **2010**, *22*, 651–655.
4. Irimia-Vladu, M.; Troshin, P. A.; Reisinger, M.; Shmygleva, L.; Kanbur, Y.; Schwabegger, G.; Bodea, M.; Schwödiauer, R.; Mumyatov, A.; Fergus, J. W.; *et al.* Biocompatible and Biodegradable Materials for Organic Field-Effect Transistors. *Adv. Funct. Mater.* **2010**, *20*, 4069–4076.
5. Legnani, C.; Vilani, C.; Calil, V. L.; Barud, H. S.; Quirino, W. G.; Achete, C. A.; Ribeiro, S. J. L.; Cremona, M. Bacterial Cellulose Membrane as Flexible Substrate for Organic Light Emitting Devices. *Thin Solid Films* **2008**, *517*, 1016–1020.
6. Hwang, S.-W.; Tao, H.; Kim, D.-H.; Cheng, H.; Song, J.-K.; Rill, E.; Brenckle, M. A.; Panilaitis, B.; Won, S. M.; Kim, Y. S.; *et al.* A Physically Transient Form of Silicon Electronics. *Science* **2012**, *337*, 1640–1644.
7. Hwang, S.-W.; Huang, X.; Seo, J.-H.; Song, J.-K.; Kim, S.; Hage-Ali, S.; Chung, H.-J.; Tao, H.; Omenetto, F. G.; Ma, Z.; *et al.* Materials for Bioresorbable Radio Frequency Electronics. *Adv. Mater.* **2013**, *25*, 3526–3531.
8. Hwang, S.-W.; Kim, D.-H.; Tao, H.; Kim, T.-I.; Kim, S.; Yu, K. J.; Panilaitis, B.; Jeong, J.-W.; Song, J.-K.; Omenetto, F. G.; *et al.* Materials and Fabrication Processes for Transient and Bioresorbable High-Performance Electronics. *Adv. Funct. Mater.* **2013**, *23*, 4087–4093.
9. Dagdeviren, C.; Hwang, S.-W.; Su, Y.; Kim, S.; Cheng, H.; Gur, O.; Haney, R.; Omenetto, F. G.; Huang, Y.; Rogers, J. A. Transient, Biocompatible Electronics and Energy Harvesters Based on ZnO. *Small* **2013**, *9*, 3398–3404.
10. Yin, L.; Cheng, H.; Mao, S.; Haasch, R.; Liu, Y.; Xie, X.; Hwang, S.-W.; Jain, H.; Kang, S.-K.; Su, Y.; *et al.* Dissolvable Metals for Transient Electronics. *Adv. Funct. Mater.* **2014**, *24*, 645–658.
11. Erogbogbo, F.; Yong, K.-T.; Roy, I.; Xu, G.; Prasad, P. N.; Swihart, M. T. Biocompatible Luminescent Silicon Quantum Dots for Imaging of Cancer Cells. *ACS Nano* **2008**, *2*, 873–878.
12. Erogbogbo, F.; Yong, K.-T.; Hu, R.; Law, W.-C.; Ding, H.; Chang, C.-W.; Prasad, P. N.; Swihart, M. T. Biocompatible Magnetofluorescent Probes: Luminescent Silicon Quantum Dots Coupled with Superparamagnetic Iron(III) Oxide. *ACS Nano* **2010**, *4*, 5131–5138.
13. Larson, D. R.; Ow, H.; Vishwasrao, H. D.; Heikal, A. A.; Wiesner, U.; Webb, W. W. Silica Nanoparticle Architecture Determines Radiative Properties of Encapsulated Fluorophores. *Chem. Mater.* **2008**, *20*, 2677–2684.
14. Park, J.-H; Gu, L.; Maltzahn, G.; Ruoslahti, E.; Bhatia, S. N.; Sailor, M. J. Biodegradable Luminescent Porous Silicon Nanoparticles for *In Vivo* Applications. *Nat. Mater.* **2009**, *8*, 331–336.
15. Low, S. P.; Voelcker, N. H.; Canham, L. T.; Williams, K. A. The Biocompatibility of Porous Silicon in Tissues of the Eye. *Biomaterials* **2009**, *30*, 2873–2880.
16. Sun, W.; Puzas, J. E.; Sheu, T. J.; Liu, X.; Fauchet, P. M. Nano- to Microscale Porous Silicon as a Cell Interface for Bone-Tissue Engineering. *Adv. Mater.* **2007**, *19*, 921–924.
17. Gatti, A. M.; Montanari, S.; Monari, E.; Gambarelli, A.; Capitani, F.; Parisini, B. Detection of Micro- and Nano-Sized Biocompatible Particles in The Blood. *J. Mater. Sci.: Mater. Med.* **2004**, *15*, 469–472.
18. Bayliss, S. C.; Buckberry, L. D.; Fletcher, I.; Tobin, M. J. The Culture of Neurons on Silicon. *Sens. Actuators* **1999**, *74*, 139–142.
19. Popescu, G.; Ikeda, T.; Dasari, R. R.; Feld, M. S. Diffraction Phase Microscopy for Quantifying Cell Structure and Dynamics. *Opt. Lett.* **2006**, *31*, 775–777.
20. Edwards, C.; Arbabi, A.; Popescu, G.; Goddard, L. L. Optically Monitoring and Controlling Nanoscale Topography during Semiconductor Etching. *Light: Sci. Appl.* **2012**, *1*, 30.
21. Pham, H. V.; Edwards, C.; Goddard, L. L.; Popescu, G. Fast Phase Reconstruction in White Light Diffraction Phase Microscopy. *Appl. Opt.* **2012**, *52*, A97–A101.
22. Maher, H.; DiSanto, D. W.; Soerensen, G.; Bolognesi, C. R.; Tang, H.; Webb, J. B. Smooth Wet Etching by Ultraviolet-Assisted Photoetching and Its Application to the Fabrication of AlGaN/GaN Heterostructure Field-Effect Transistors. *Appl. Phys. Lett.* **2000**, *77*, 3833–3835.
23. Minsky, M. S.; White, M.; Hu, E. L. Room-Temperature Photoenhanced Wet Etching of GaN. *Appl. Phys. Lett.* **1996**, *68*, 1531–1533.
24. Cho, H.; Auh, K. H.; Han, J.; Shul, R. J.; Donovan, S. M.; Abemathy, C. R.; Lambers, E. S.; Ren, F.; Pearton, S. J. UV-Photoassisted Etching of GaN in KOH. *J. Electron. Mater.* **1999**, *28*, 290–294.
25. Van de Ven, J.; Nabben, H. J. P. Photo-assisted Etching of p-Type Semiconductors. *J. Electrochem. Soc.* **1991**, *138*, 3401–3406.
26. Seidel, H.; Csepregi, L.; Heuberger, A.; Baumgartel, H. Anisotropic Etching of Crystalline Silicon in Alkaline Solutions I. Orientation Dependence and Behavior of Passivation Layers. *J. Electrochem. Soc.* **1990**, *137*, 3612–3626.
27. Seidel, H.; Csepregi, L.; Heuberger, A.; Baumgartel, H. Anisotropic Etching of Crystalline Silicon in Alkaline Solutions II. Influence of Dopants. *J. Electrochem. Soc.* **1990**, *137*, 3626–3632.
28. Bhrany, A. D.; Irvin, C. A.; Fujitani, K.; Liu, Z.; Ratner, B. D. Evaluation of a Sphere-Templated Polymeric Scaffold as a Subcutaneous Implant. *JAMA Facial Plast. Surg.* **2013**, *15*, 29–33.